CCFE
CULHAM CENTRE FOR FUSION ENERGY

UK Atomic Energy Authority

UKAEA-CCFE-PR(23)153

P.-Y. Li, D. R. Hatch, B. Chapman-Oplopoiou, S. Saarelma, C. M. Roach, M. Kotschenreuther, S. M. Mahajan, the MAST Team

ETG Turbulent Transport in the Mega Ampere Spherical Tokamak (MAST) Pedestal

ETG Turbulent Transport in the Mega Ampere Spherical Tokamak (MAST) Pedestal

P.-Y. Li, D. R. Hatch, B. Chapman-Oplopoiou, S. Saarelma, C. M. Roach, M. Kotschenreuther, S. M. Mahajan, the MAST Team

This is a preprint of a paper submitted for publication in Nuclear Fusion

ETG Turbulent Transport in Mega Ampere Spherical Tokamak (MAST) Pedestal

P.-Y. Li[1], D. R. Hatch[1], B. Chapman-Oplopoiou[2], S. Saarelma[2], C. M. Roach[2], M. Kotschenreuther[1], S. M. Mahajan[1], and the MAST Team

[1] *Institution for Fusion Studies, The University of Texas at Austin, Austin, TX, USA.*

[2] *UKAEA CCFE, Culham Science Centre, Abingdon, Oxon, UK.*

Abstract

The results of a recent gyrokinetic analysis of turbulent transport driven by the electron temperature gradient (ETG) in the MAST pedestal are presented. During the inter-ELM period, the buildup rate of the electron density gradients is faster than that of the electron temperature gradients, possibly indicating the presence of an active electron thermal transport mechanism. Local nonlinear simulations from the gyrokinetic code, GENE, show that heat flux produced by ETG turbulence is 10-30% of the total applied heating power in the upper pedestal and pedestal top during both the pre-ELM (80-99% inter-ELM period) and post-ELM (0-20%) periods. Increasing strongly with the electron temperature gradient, the ETG transport appears to be stiff. Considering radiation losses, ion thermal transport, and the strong sensitivity of the transport to the electron temperature gradient, we propose that ETG transport is a plausible mechanism mediating the inter-ELM temperature profile on MAST. Cognizant of the fact that the profiles may depart considerably from a linear approximation, we conducted global nonlinear simulations; the results are in good agreement with local simulations except near the pedestal top, where large streamers and high transport levels (far beyond experimental) develop in the local simulations. This study is a warning that when the profiles have deep structures, local simulations must be augmented /checked by global ones. We quantify and parameterize the discrepancy between local and global simulations by calculating the ratio of the radial correlation length to a length scale representative of the profile curvature. When this ratio is sufficiently small, local and global simulations agree as expected.

1 Introduction

In tokamaks, including the Mega Ampere Spherical Tokamak (MAST), a narrow transport barrier that improves the confinement of magnetized plasma is formed in the high confinement mode (H mode) [2]. This barrier supports high density and temperature gradients at the edge of the plasma, which leads to the development of a steep pressure pedestal. In MAST, this pedestal undergoes a cyclical process of growth and collapse by an edge-localized mode (ELM) [3]. During this process, the electron density pedestal builds up much faster than the electron temperature pedestal, suggesting that an electron thermal transport mechanism may be active and constraining the inter-ELM pedestal evolution. This paper uses the gyrokinetic code, GENE [4], to investigate the role of electron temperature gradient (ETG) driven turbulent transport in the MAST pedestal.

Historically, it was believed that ETG turbulence would not significantly affect transport due to low transport levels predicted by simple mixing length estimates. However, nonlinear gyrokinetic simulations have shown that the formation of radially-extended structures, also known as streamers, in the nonlinear turbulent state can potentially lead to significant ETG transport in both conventional tokamaks [4, 5, 6]. Recent work has determined that ETG can produce substantial transport in the pedestal [1, 7, 8, 9, 10, 11, 12, 13]. Typically the ETG transport in the pedestal does not rely on streamers. Rather, the fluctuations remain relatively isotropic [8, 14] and achieve substantial heat fluxes due to the extreme pedestal gradients.

This paper presents linear and nonlinear, local and global gyrokinetic analyses of ETG in the MAST pedestal. Simulations produce ETG turbulence at experimentally-relevant transport levels with transport increasing rapidly with $\eta = L_n/L_T$ (i.e., the transport is stiff), where $L_{n,T}$ are the electron density and temperature gradient scale lengths, respectively. This is the case during both pre-ELM (80-99% inter-ELM period) and post-ELM (0-20%) periods in the pedestal top and upper pedestal region. We conclude that ETG turbulence likely plays a significant role in electron thermal transport in the MAST pedestal. This ETG transport

likely acts together with microtearing modes (MTM), which have been studied previously [15], to constrain the electron temperature pedestal, while pressure gradient is constrained by KBM and the total pedestal pressure is limited by the ideal MHD peeling-ballooning modes.[15, 16]. The combination of ETG and MTM has also been identified in standard aspect ratio pedestals [9, 10, 17, 18, 19].

We also study various aspects of the fundamental nature of the turbulent energetics, finding that energy is injected at low radial wavenumbers and high bi-normal wavenumbers and then transferred via a direct cascade in the radial direction and an inverse cascade in the bi-normal direction.

Since ETG fluctuates at such small scales, a local approximation is typically thought to be adequate even for the exceptionally steep gradients in the pedestal. We test this assumption explicitly by comparing local and global nonlinear simulations. This comparison is particularly relevant for the MAST pedestal due to its comparatively weak magnetic field (compared to comparable standard aspect ratio tokamaks), which results in weaker scale separation between gyro-radius scales and equilibrium scales. We find close agreement at most locations, but substantial deviation in the region where the density profile transitions from the pedestal to the core (i.e. where profile curvature is large). In this region, local simulations produce anomalously large transport levels. In contrast, global simulations produce realistic transport levels in line with the other radial positions. These findings provide insight into the mechanisms behind the formation of the pedestal. Ultimately the goal is to enable improved confinement in spherical tokamaks.

The presentation of the results is organized as follows. In Sec. 2, ETG turbulence is shown to be active according to local linear and nonlinear pre-ELM simulations, sensitivity tests for linear and nonlinear gyrokinetic simulations are conducted by varying the density and temperature gradients, global nonlinear gyrokinetic simulations are compared to local simulations at different radial locations, and it is shown that ETG turbulence can be affected by global properties. Local post-ELM simulations are presented and compared to pre-ELM

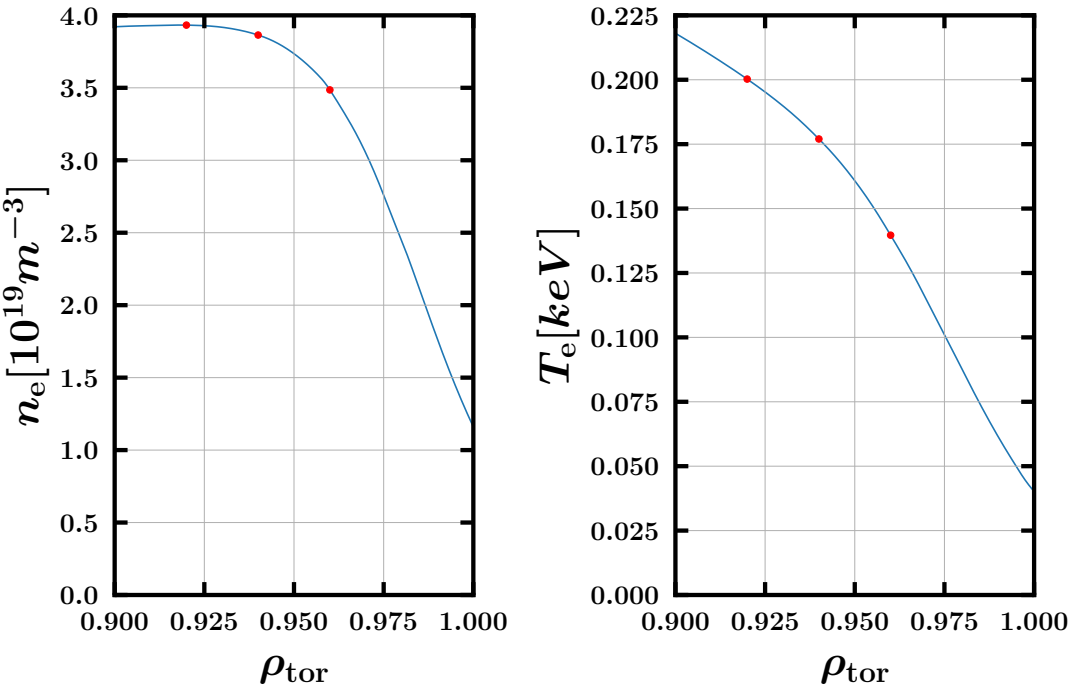

Figure 1: The electron density and temperature versus the normalized toroidal flux surface label $\rho_{\rm tor}$ during pre-ELM stage.

ρ_{tor}	q_0	$\hat{s}$	$\omega_{\rm n}$	$\omega_{\rm T}$	η	β	$B_{\rm ref}$	$T_{\rm ref}$	$n_{\rm ref}$	ρ^*
0.92	5.41	4.16	0.126	4.86	38.6	0.0136	0.483	0.200	3.93	0.00499
0.94	5.92	4.14	2.16	8.13	3.79	0.0118	0.483	0.177	3.86	0.00469
0.96	6.46	4.20	9.71	16.7	1.72	0.0084	0.483	0.140	3.48	0.00416

Table 1: The common physical input parameters at $\rho_{\rm tor} = 0.92, 0.94, 0.96$, respectively. η and β decrease as $\rho_{\rm tor}$ increases. Magnetic shear does not vary a lot around the pedestal top.

simulations in Sec. 3. Energy triplet diagnostics and energy across the scale are studied to understand how ETG turbulence saturates in MAST at different stages in Appendix A for futher readings. The simulation setups for the nonlinear simulations will be presented in Appendix B.

2 Local Pre-ELM Simulations

In order to check whether ETG turbulence is important in the pedestal, we begin by looking at the region around the pedestal top where $\eta = L_{\rm n}/L_{\rm T}$, the ratio of density scale length

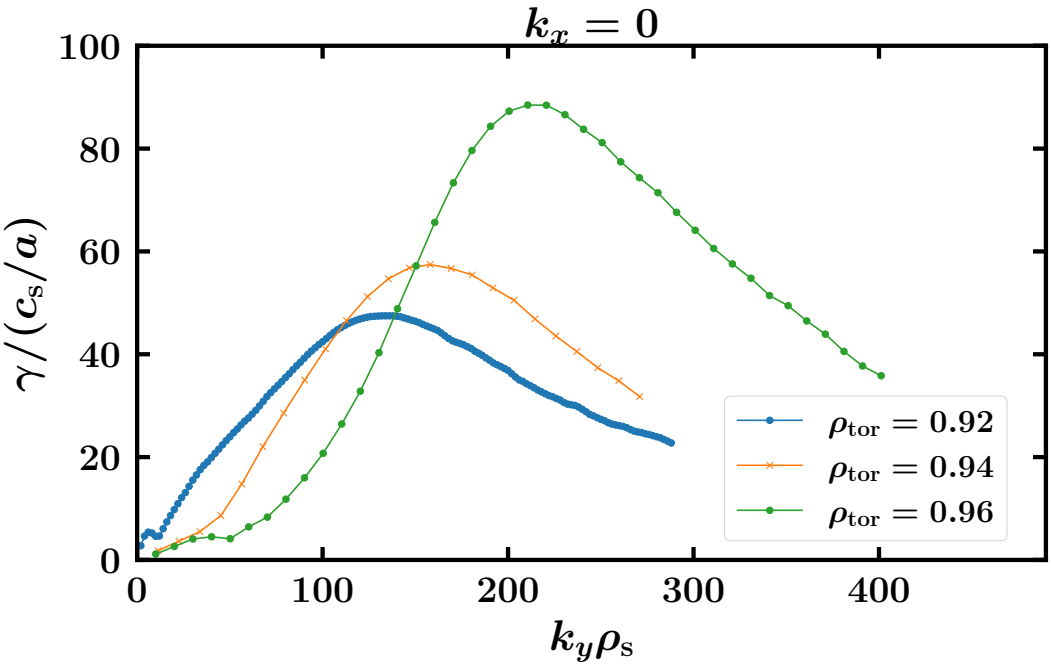

Figure 2: Growth rate spectrum γ versus $k_y\rho_s$ during pre-ELM stage with c_s and ρ_s calculated at $\rho_{tor} = 0.92$. Growth rate spectrum peaks at a smaller scale for the outer radial location for similar k_x, implying the heat flux can be smaller for larger ρ_{tor} based on simple mixing length estimates.

and temperature scale length, is large.

As shown in Fig. 1, three radial locations at $\rho_{tor} = 0.92, 0.94, 0.96$ are picked to cover the pedestal top for the test during the pre-ELM stage. We focus particularly on this upper pedestal region since transport is found to be low from ETG at $\rho_{tor} = 0.96$ already as shown later, the steep gradient region with even smaller η and T_{ref} is therefore not a region of interest.

The radial coordinate, ρ_{tor}, is the square root of normalized toroidal flux. Table 1 shows the physical input parameters for the simulations where normalized density gradient $\omega_{n_e} = \omega_{n_i} = \omega_n = a/L_n$, normalized temperature gradient $\omega_{Te} = \omega_{Ti} = \omega_T = a/L_T$, the normalized plasma pressure $\beta = 8\pi n_{e0} T_{ref}/B_{ref}^2$, the safety factor q_0, the normalized magnetic shear $\hat{s} = \frac{r}{q}\frac{dq}{dr}$, reference magnetic field in Tesla B_{ref}, reference temperature in keV T_{ref}, reference density in $10^{19} m^{-1}$, and the ratio ion gyroradius and minor radius ρ^*. Also

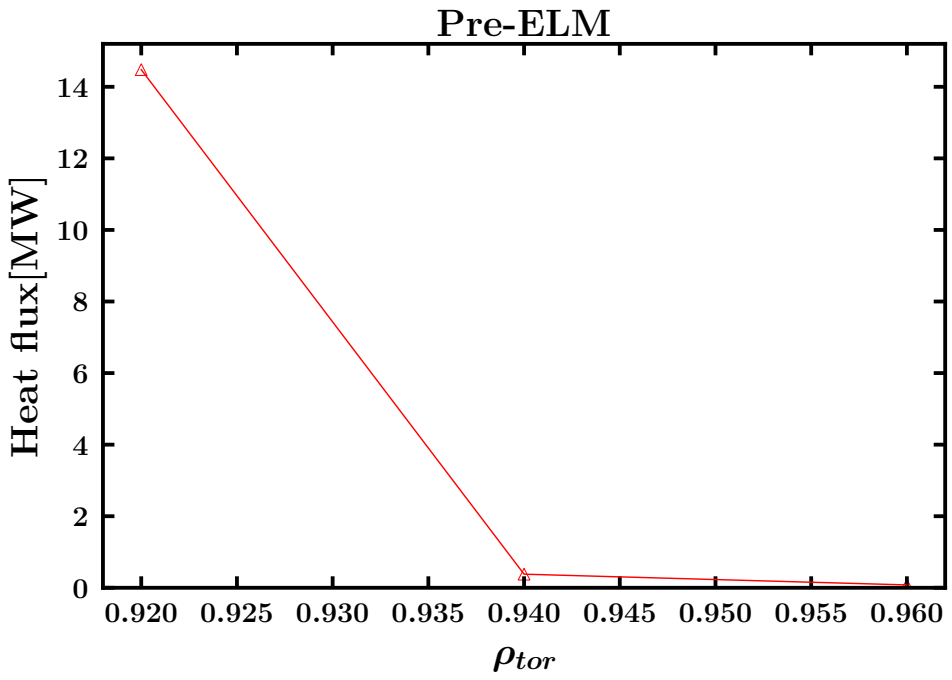

Figure 3: Heat fluxes calculated at $\rho_{\rm tor} = 0.92, 0.94$, and 0.96 are 14.48, 0.38, and 0.08MW, respectively. With regard to the 3.2MW NBI power of MAST, the local nonlinear simulation predicts inaccurate heat flux, global effects need to considered.

note that a and R are the minor and major radii, respectively, the effective ion charge Z_{eff} is set to 2, and the ion and electron temperatures and densities are set equal for all simulations.

Figure 2 shows the growth rate spectrum, growth rate γ versus binormal wavenumber $k_y\rho_s$, calculated at different radial locations with linear gyrokinetic initial value runs centered at the outboard mid-plane, where ρ_s is the ion gyroradius and $c_{\rm s}$ is the ion sound speed. Note that $\hat{e}^x$, $\hat{e}^y$, and $\hat{e}^z$ are radial, binormal, and tangent unit vector in GENE convention, respectively.

Table 2 shows some of the important characteristic values of the most unstable modes (electron scales) at three radial locations used to categorize the instabilities. In this table, ω is the real frequency, χ is the heat diffusivity, and D is the particle diffusivity. These instabilities are highly electrostatic electron waves with low particle flux, which of course can be identified as ETG modes [20]. One interesting observation from Fig. 2 is that the peak of the growth rate spectrum moves to a smaller scales as the radial location moves

$\rho_{\rm tor}$	$k_y\rho_{\rm s}$	$\gamma(c_{\rm s}/a)$	$\omega(c_{\rm s}/a)$	$\chi_{\rm em}/\chi_{\rm es}$	$\chi_{\rm i}/\chi_{\rm e}$	$D_{\rm e}/\chi_{\rm e}$
0.92	136	47.5	-137.1	-1.24×10^{-3}	1.27×10^{-3}	-0.161
0.94	168	60.4	-134.8	-1.06×10^{-3}	1.07×10^{-2}	-7.5×10^{-3}
0.96	252	105.9	-144.5	4.62×10^{-4}	2.36×10^{-2}	5.12×10^{-3}

Table 2: Charateristic values for the most unstable mode at three different radial locations. Low $\chi_{\rm em}/\chi_{\rm es}$, low $\chi_{\rm i}/\chi_{\rm e}$, and small $D_{\rm e}/\chi_{\rm e}$ imply that these instabilities are electrostatic, electron dominant, and have low particle flux,a respectively. Therefore, these instabilities are ETG modes.

outward. A simple mixing length estimate (not shown), $\chi \sim \gamma/k_y^2$, would predict that the thermal diffusivity would decrease as the radial location increases (for example, note that the peak k_y approximately doubles as does the peak growth rate comparing $\rho_{tor} = 0.92$ and $\rho_{tor} = 0.96$). This quick assessment is confirmed by the nonlinear simulations described below with the numerical info included in Appendix B.

Figure 3 shows the heat fluxes derived from local nonlinear gyrokinetic simulations at three different radial locations in megawatts. The simulations include E × B shear and $k_{y\rm min}\rho_{\rm s}$ is set as 6. The heat flux is calculated to be 14.48MW at $\rho_{\rm tor} = 0.92$, which is far higher than the heat fluxes 0.38MW and 0.08MW calculated at $\rho_{\rm tor} = 0.94$ and 0.96, respectively. This discharge is heated by NBI at a level of 3.2 MW. Although a detailed analysis is not available, some fraction of the heating power is lost as radiation, some fraction is also transported through the ion channel, and some of the energy is transported when the pedestal collapses in ELMs. We will proceed by assuming that something on the order of 1 MW is a plausible expectation for electron thermal transport. Note that the pedestal profiles are not in a fully steady state but are evolving between ELMs. Based on this assumption, only the result at $\rho_{tor} = 0.94$ is in the proximity of experimental expectations. However, we as will be shown below, all three radial positions plausibly produce reasonable transport levels when global effects and/or parameter sensitivities are considered. More specifically, global effects bring the transport at $\rho_{tor} = 0.92$ in line with experimental expectations, and the transport at $\rho_{tor} = 0.96$ becomes experimentally relevant when density and temperature gradients are slightly modified.

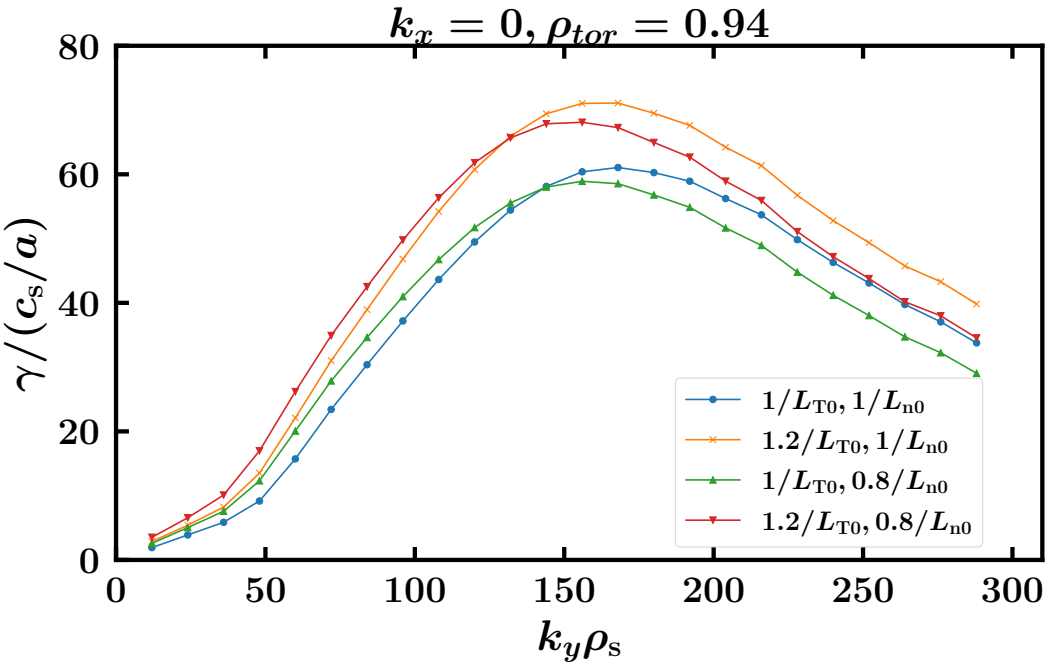

Figure 4: Growth rate spectrum at $\rho_{\rm tor} = 0.94$ during the pre-ELM stage. The spectrum is moved upward about 20% when the temperature gradient $1/L_{\rm T0}$ is increased by 20%, and moved horizontally toward the larger scale when $1/L_{\rm n0}$ s decreased.

Due to the typical extreme sensitivity of turbulent transport to gradients, a thorough investigation must probe experimental uncertainties in the profiles. The profiles used for the simulations averaged over several ELM cycles. Although rigorous uncertainties are difficult to quantify, the error bar of the gradients can exceed 20%. It is then reasonable to vary the gradients within this range in order to check what is the highest heat flux the instabilities can produce and how stiff the transport is.

Figure 4 shows how the growth rate spectrum changes when the density and temperature gradients are varied at $\rho_{\rm tor} = 0.94$ during the pre-ELM stage. When the temperature gradient $1/L_{\rm T0}$ is increased by 20%, the growth rates at all scales are also increased by approximately 20%, which is typical for ETG turbulence. On the other hand, when the density gradient $1/L_{\rm n0}$ is decreased by 20%, the growth rate spectrum is not shifted upward, instead, it is shifted toward the larger scales. The case with 20% increase in $1/L_{\rm T0}$ and 20% decrease

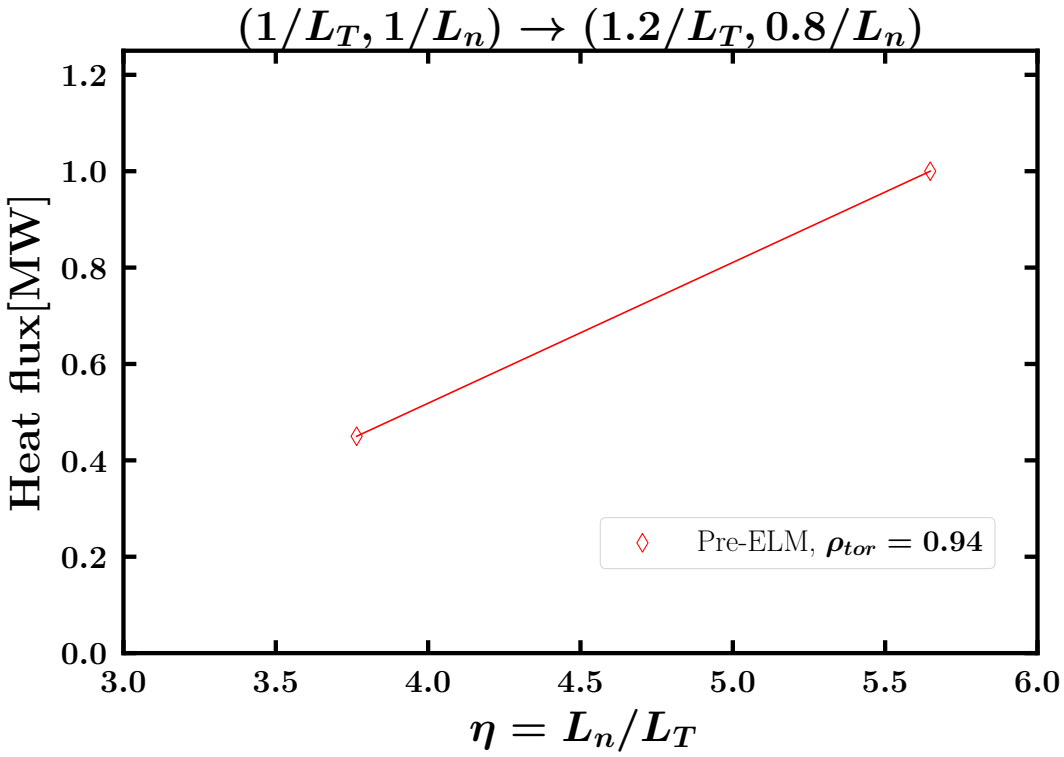

Figure 5: Heat fluxes calculated at $\rho_{\rm tor} = 0.94$ for the pre-ELM stage shows the heat flux increased significantly when there is a 20% increase in $1/L_{\rm T0}$ and a 20% decrease in $1/L_{\rm n0}$. The amount of heat flux increased is more profound than the result got from linear simulations.

in $1/L_{\rm n0}$ has the spectrum moved toward the up-left corner with $\sim$ 40% of growth rates increase in the larger scales, which are more important for transport. This result suggests ETG turbulence does not depend solely on $\eta = L_{\rm n}/L_{\rm T}$, its growth rate is more responsive to the change of the temperature gradient. The heat fluxes obtained from nonlinear gyrokinetic simulations in the pre-ELM stage at radial locations of $\rho_{\rm tor} = 0.94$ is shown in Fig. 5. The simulations reveal that the heat flux increases significantly when there is a 20% increase in $1/L_{\rm T0}$ and a 20% decrease in $1/L_{\rm n0}$. Specifically, the pre-ELM case shows a 110% increase in heat flux. We note that this increase is much higher than the corresponding increase in the maximum growth rates, which exhibit an increase of only $\sim$ 40%. The results suggest that ETG turbulence is highly sensitive to the gradients, and even a slight increase in the pedestal temperature can lead to significant heat flux changes. These results also highlight

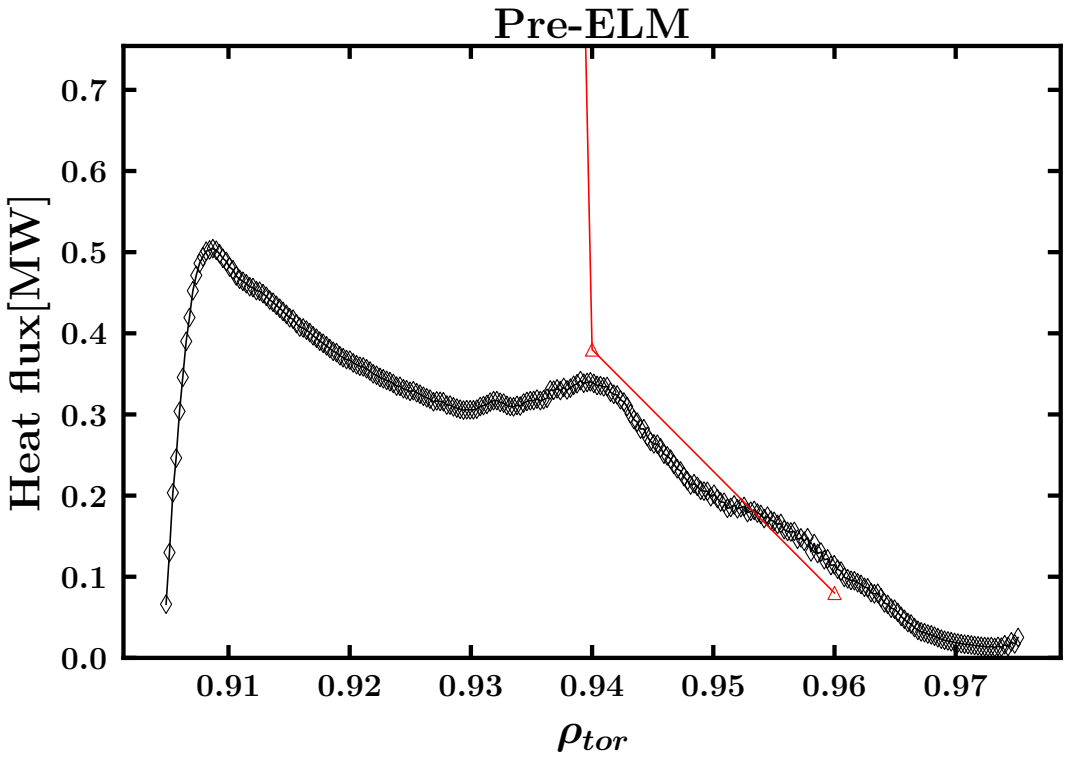

Figure 6: The heat fluxes calculated at $\rho_{\rm tor} = 0.94$ and 0.96 agree with the result derived from global simulation with minor differences while those at $\rho_{\rm tor} = 0.92$ and 0.93 are way off, implying that the global effects can be crucial.

the importance of investigating how ETG turbulence in the pedestal top for STs saturates, and suggests that deeper investigation into the nonlinear effects is needed.

2.1 Nonlocal Effects

We return now to the exceptionally high heat flux predicted at $\rho_{\rm tor} = 0.92$ (see Fig. 3), which far exceeds the total heating power for this discharge. The growth rates at the lower k_y wavenumbers, shown in Fig. 2, significantly surpass those at $\rho_{\rm tor} = 0.94$ and 0.96. Even so, the unrealistically large heat flux is not expected from simple mixing length estimates derived from the growth rate spectrum. We investigate the possibility that nonlocal effects are necessary to recover reasonable transport levels.

Figure 6 displays the calculated global heat flux versus the local results with an extra

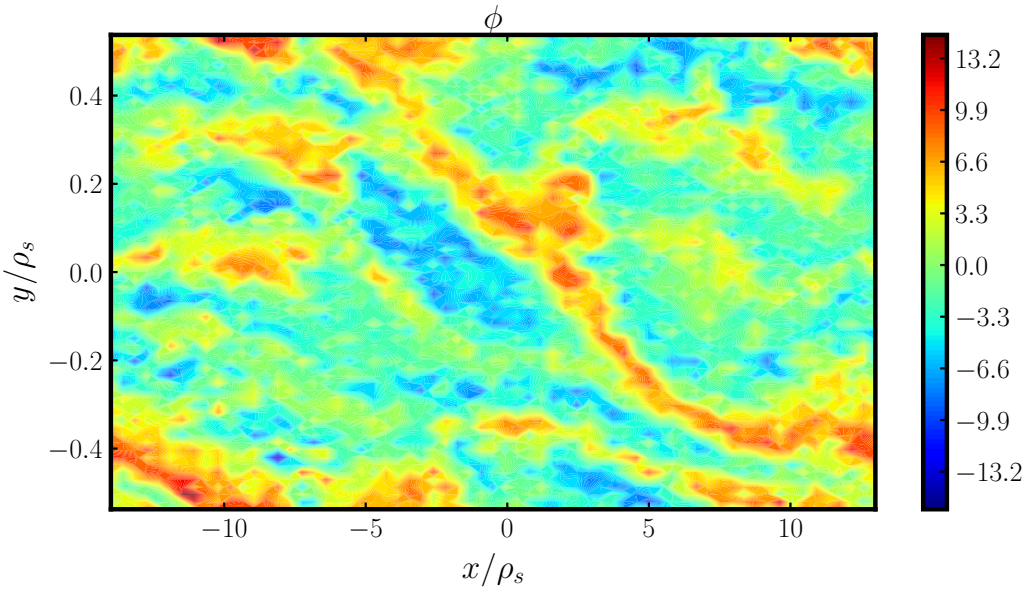

Figure 7: A time slice of the electrostatic potential for the nonlinear local simulation at $\rho_{\text{tor}} = 0.92$. The extended structure suggests that the dominant instabilities at $\rho_{\text{tor}} = 0.92$ could be affected by the radial structure and properties in nonlinear global simulations.

local simulation at $\rho = 0.93$. While the heat fluxes at $\rho_{\text{tor}} = 0.94$ and 0.96 agree with the result obtained from the global simulation, with minor differences, those at $\rho_{\text{tor}} = 0.92$ and 0.93, with $Q_{es} = 14.48$ and 6.62MW, respectively, are far off. The heat fluxes calculated from global simulation at $\rho_{\text{tor}} = 0.92$ and 0.93 fall within the experimental expectation, indicating that global effects significantly reduce the heat flux at these locations.

Global and local simulations differ in terms of whether they incorporate the radial variation of profiles and equilibrium. Additionally, it is important to highlight that the boundary conditions employed in local and global simulations also vary. Local simulations utilize periodic boundary conditions, while global simulations utilize a combination of Dirichlet and Neumann boundary conditions. To assess the impact of boundary conditions on heat flux transport at the top of the pedestal, the convergence check involves modifying the box size, effectively ruling out the influence of boundary conditions. In order to assess the importance of global effects from the radial variation of the profiles, it is necessary to examine the radial structure of turbulence in the local simulation. Here, we present the results of local

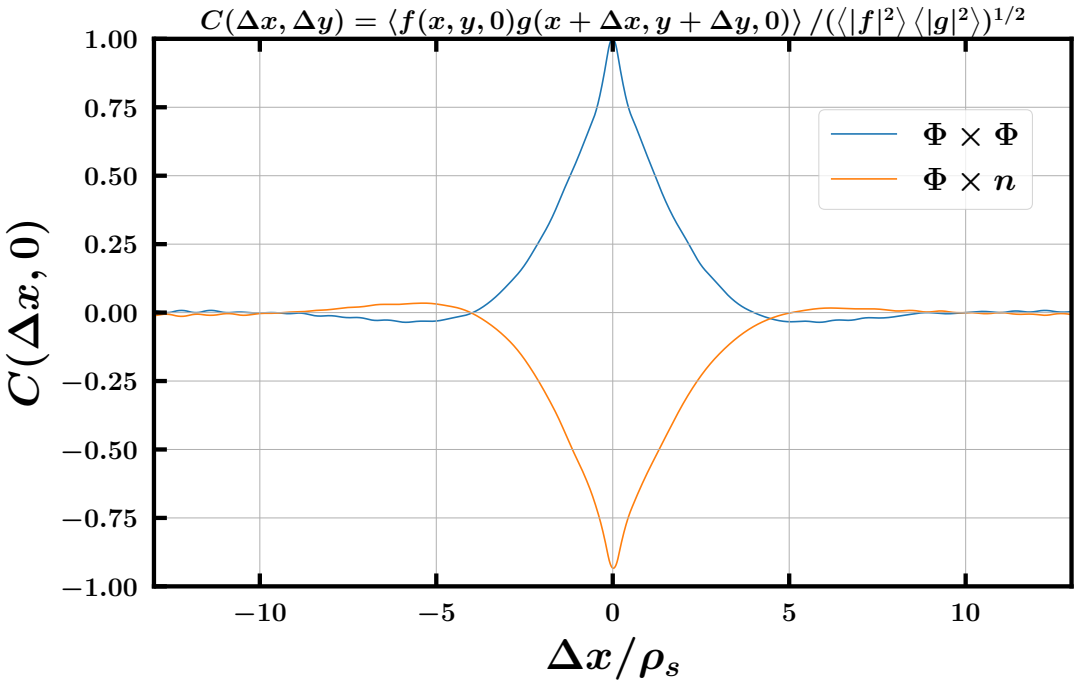

Figure 8: The cross-correlations $C(\Delta x, 0)$ of $\Phi - \Phi$ and $\Phi - n$ derived from the nonlinear local simulation at $\rho_{\rm tor} = 0.92$. The half-width for both is around $1.5\rho_s$ or $0.0075\rho_{\rm tor}$. $C(\Delta x, 0)$ drops to 0.25 when Δx reaches $2\rho_s$ or $0.01\rho_{\rm tor}$. The size of the relevant region is large enough to include strongly varying η regions in global simulations.

nonlinear simulations during the saturated state, where the box size L_x is set to $27\rho_s$. Note that to saturate the turbulence, $L_x = 13.5\rho_s$ is shown to be sufficient in the convergence test. Since $\rho^*_{\rm ref} = \rho_s/a = 0.00499$, the equivalent box size as a fraction of the minor radius a is 0.136, which is substantially larger than the entire pedestal (recall Figure 1). Figure 7 shows the time slice of the Φ contour plot in real space. The extended structure seen in the figure, combined with the fact that the simulation is located at $\rho_{\rm tor} = 0.92$, suggests that the dominant instabilities in the local simulation could potentially be affected by the global properties across the whole pedestal top and upper pedestal region—e.g. the structures are broad enough that they would extend to the regions ($\rho_{tor} > 0.93$) of much smaller local heat flux. To further investigate the radial structure of turbulence centered at $\rho_{\rm tor} = 0.92$, we examine the cross-correlations $C(\Delta x, 0)$ of $\Phi - \Phi$ and $\Phi - n$ as shown in Figure 8. The half-width of $C(\Delta x, 0)$ is about $1.5\rho_s$ or $0.0075\rho_{\rm tor}$. It first reaches 0 when Δx becomes $4\rho_s$

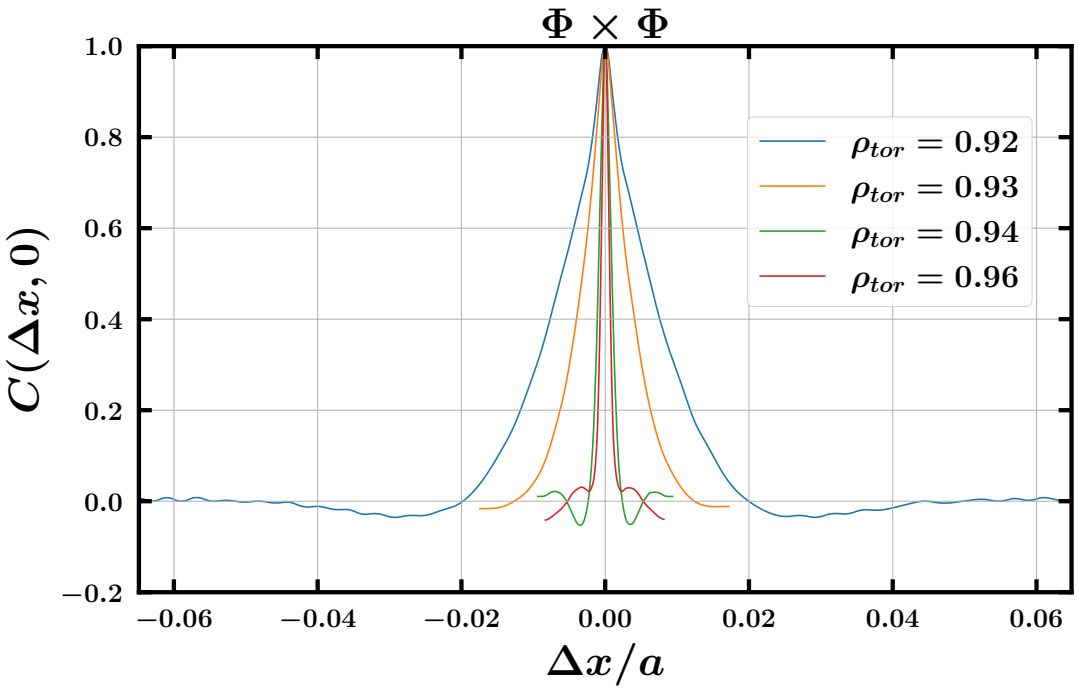

Figure 9: The cross-correlations $C(\Delta x, 0)$ of $\Phi - \Phi$ derived from the nonlinear local simulations for $\rho_{\rm tor} = 0.92$, 0.93, 0.94, and 0.96. The half-widths of $C(\Delta x, 0)$ are several times smaller for $\rho_{\rm tor} = 0.94$ and 0.96 compared to 0.92 and 0.93.

or $0.02\rho_{\rm tor}$, suggesting that the most relevant range for the turbulence would be $0 \sim .90$ to ~ 0.94.

Figs. 9 and 10 show the cross-correlations at several radial positions. At $\rho_{\rm tor} = 0.94$ and 0.96 the correlation lengths are much smaller compared to those at 0.92 and 0.93, which is consistent to the result that the local approximation is more accurate compared to the global result at these two locations.

Considering the impact of these observations on the turbulent properties, we refer to Fig. 1 and Tab. 1. The results show that the temperature and density profiles (and η) decrease significantly as $\rho_{\rm tor}$ is pushed outward within the range of 0.90 to 0.94. This decrease will inevitably weaken the ETG turbulence. On the other hand, other parameters such as the safety factor q and magnetic shear $\hat{s}$ vary weakly within this range and are therefore unlikely to explain the discrepancy between the global and local simulations.

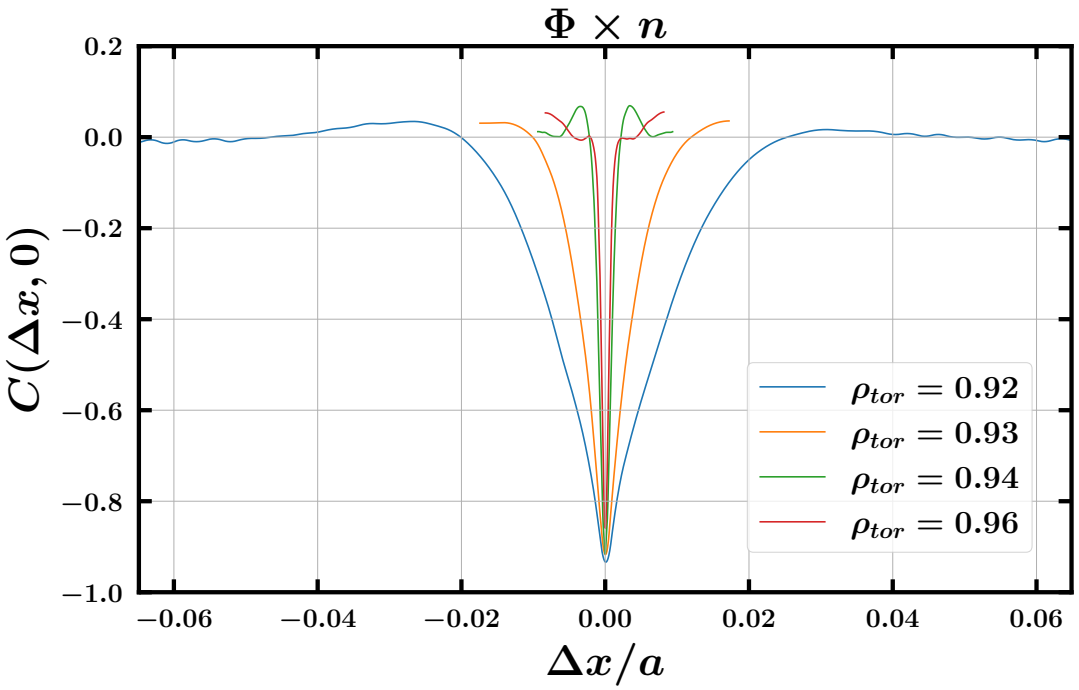

Figure 10: The cross-correlations $C(\Delta x, 0)$ of $\Phi - n$ derived from the nonlinear local simulations for $\rho_{\rm tor} = 0.92$, 0.94, and 0.96. Similar to the $\Phi - \Phi$ case, the half-widths of $C(\Delta x, 0)$ are several times smaller for $\rho_{\rm tor} = 0.94$ and 0.96 compared to 0.92 and 0.93.

2.2 The effect of $E \times B$ shear

Another possible relevant mechanism is $E \times B$ shear suppression. Often flow shear is assumed to have little effect on ETG turbulence due to its small scales in time and space. However, the large radial structures observed in the pedestal top simulations may make them more susceptible to shear suppression. We note that all simulations described above include $E \times B$ shear. However, there is substantial uncertainty in the shear rate and so we conduct scans to probe sensitivities. The E × B shearing rate $\gamma_{\rm E\times B}$ exhibits significant variability across the pedestal region, as illustrated in Fig. 11, where the $\gamma_{\rm E\times B}$ has been estimated from a neoclassical formula [21] by setting the parallel flow $V_{\|}$ to zero, which is the same procedure adopted in [13]. At $\rho_{\rm tor} = 0.92$, the shearing rate is only 0.058, but increases by a factor of ~ 5 at $\rho_{\rm tor} = 0.93$ and by a factor of ~ 10 at $\rho_{\rm tor} = 0.94$. While these values may appear small for electron-scale turbulence, they are more comparable to the growth rates of ion-

scale turbulence, which has the potential to reduce heat flux. To investigate this, nonlinear simulations were conducted for $\rho_{\rm tor} = 0.92$, and Fig. 12 shows the corresponding $\gamma_{\rm E\times B}$ scans. The results reveal that the heat flux decreases significantly as $\gamma_{\rm E\times B}$ increases, with an 85% reduction observed when $\gamma_{\rm E\times B}$ increases by a factor of 10. As $\gamma_{\rm E\times B}$ is increased further, the heat flux can be suppressed even more, potentially reaching a value of 0.54MW when $\gamma_{\rm E\times B}$ is equal to 2.5. It is worth noting that these values for $\gamma_{\rm E\times B}$ were chosen as approximations of the shearing rate at $\rho_{\rm tor} = 0.94$ (the boundary of the highly correlated region) and 0.96 (the simulated boundary), in order to investigate the possible maximum effect of shearing on turbulence.

2.3 Parameterizing the Breakdown of the Local Flux Tube Approximation

The above analysis shows the ETG turbulence in the pedestal top for MAST can be affected by the global properties, which is also shown for some systems with ETG turbulence [22]. The background magnetic fields of spherical tokamaks are mostly less than 1T with $\sim 0.5T$ in our case for MAST, which is much weaker than most cases for conventional tokamaks. The weaker magnetic field results in larger normalize gyroradius $\rho_* = \rho_s/a$ and therefore leads comparatively larger fluctuation scales. Combined with the fact that the pedestal is intrinsically narrow, the size of the pedestal top transition region then becomes only $\sim 5\rho_s$. Therefore, the fluctuations with extended radial structure in the local simulations in this region are not going to be as prominent in global simulations because the simulated region covers a large variety of gradients and $\gamma_{\rm E\times B}$.

The aforementioned analysis provides a qualitative explanation, but it is imperative to conduct quantitative assessments to ascertain the validity of the local approximation. The local flux tube approximation firstly assumes the density gradient scale length, denoted as $L_n = \frac{n}{dn/dx}$, and the temperature gradient length scale, denoted as $L_T = \frac{T}{dT/dx}$, can be approximated as constants across the simulated region, and then secondly employs periodic boundary conditions. We define the correlation length in the radial direction, Δ_x, as the

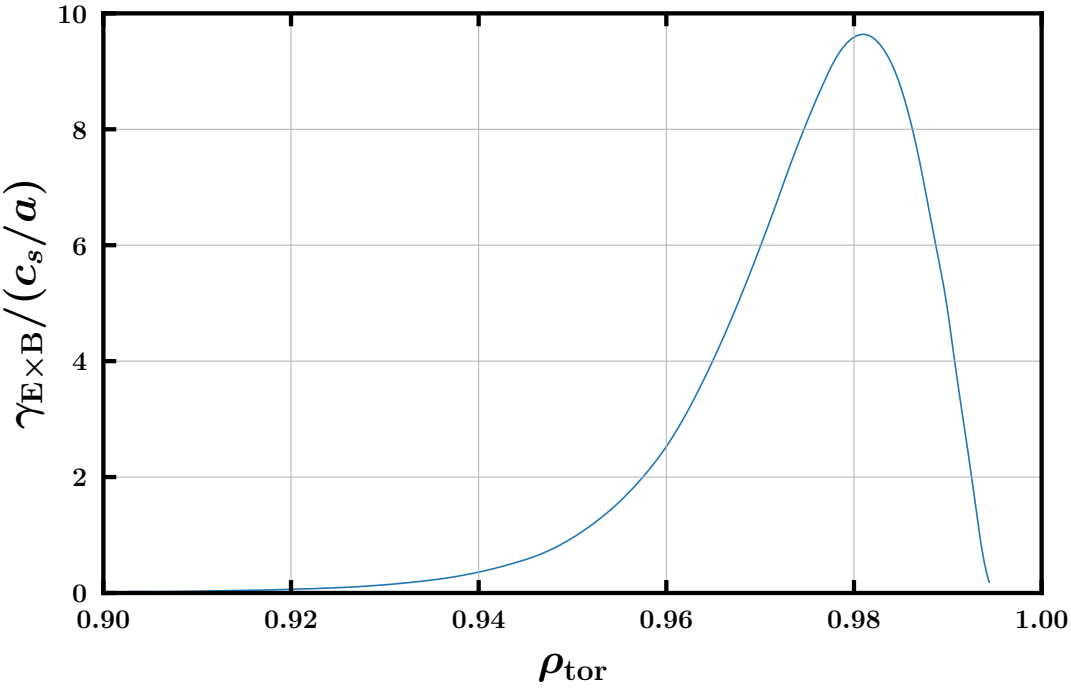

Figure 11: The E × B shearing rate $\gamma_{\mathrm{E\times B}}$ is nearly zero in the pedestal top and becomes significantly larger at the upper and mid pedestal region. Instabilities with extended structure in radial direction emerged in local simulations in the pedestal top can be affected by the shear.

width of $C(\Delta x, 0)$ that first crosses zero, as illustrated in Fig. 9. To evaluate its significance in relation to other length scales, the density profile is initially investigated to verify the fulfillment of various relevant conditions.

Expanding $\frac{\nabla n}{n}(x)$ to the first order, $\frac{\nabla n_0}{n_0} + x\frac{n_0\nabla^2 n_0 - (\nabla n_0)^2}{n_0^2}$, it becomes apparent that the correlation length in the radial direction, Δ_x, must satisfy the first condition $\Delta_x \ll |\frac{\nabla n_0}{n_0}|$ $/|\frac{n_0\nabla^2 n_0 - (\nabla n_0)^2}{n_0^2}|$ when approximating $\frac{\nabla n}{n}(x)$ with $\frac{\nabla n_0}{n_0}$. Conversely, Δ_x should also be smaller than L_n and L_T to ensure the validity of the periodic boundary condition, specifically $|\Delta_x/L_n|$ and $|\Delta_x/L_T| \ll 1$ as the second condition. The local approximation breaks down if any of the aforementioned conditions is violated. The outcome of the first condition is depicted in Figure 13 , where it is evident that the condition is violated at $\rho_{\mathrm{tor}} = 0.92$ and 0.93, while being satisfied at $\rho_{\mathrm{tor}} = 0.94$ and 0.96. Although this does not provide insights into how turbulence is affected by higher-order terms, it directly indicates the breakdown of the local

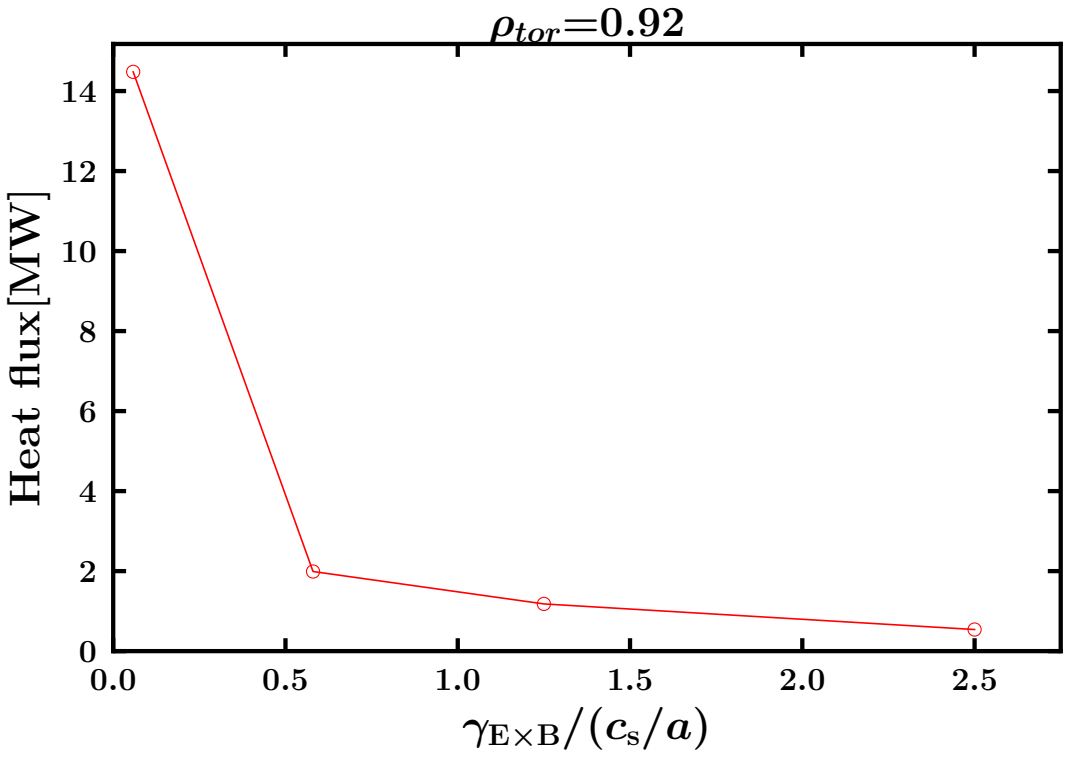

Figure 12: Heat flux versus the E × B shearing rate $\gamma_{\mathrm{E\times B}}$. Heat flux decreases significantly as $\gamma_{\mathrm{E\times B}}$ increases, with a 85% decrease when $\gamma_{\mathrm{E\times B}}$ becomes 10 times larger. The heat flux can eventually reach a physical value of 0.54MW when $\gamma_{\mathrm{E\times B}}$ is equal to 2.5.

approximation at these radial locations due to profile curvature. The second condition and a similar analysis for T exhibit satisfactory fulfillment at these radial positions but is not presented here.

We note that this analysis points to the significant role played by the curvature of the density profile, denoted as $\nabla^2 n$, in determining the validity of the local approximation. In the absence of the curvature term, the first and second conditions are mathematically equivalent, and their fulfillment is observed across all cases examined in this study. This finding suggests that the curvature of the profiles can significantly influence the turbulent transport, in particular by stabilizing the ETG modes in this case. An interesting analysis would be to explore the second order curvature effects described Refs. [26, 27]. However, the precise manner in which the curvature of the profiles impacts different micro-instabilities

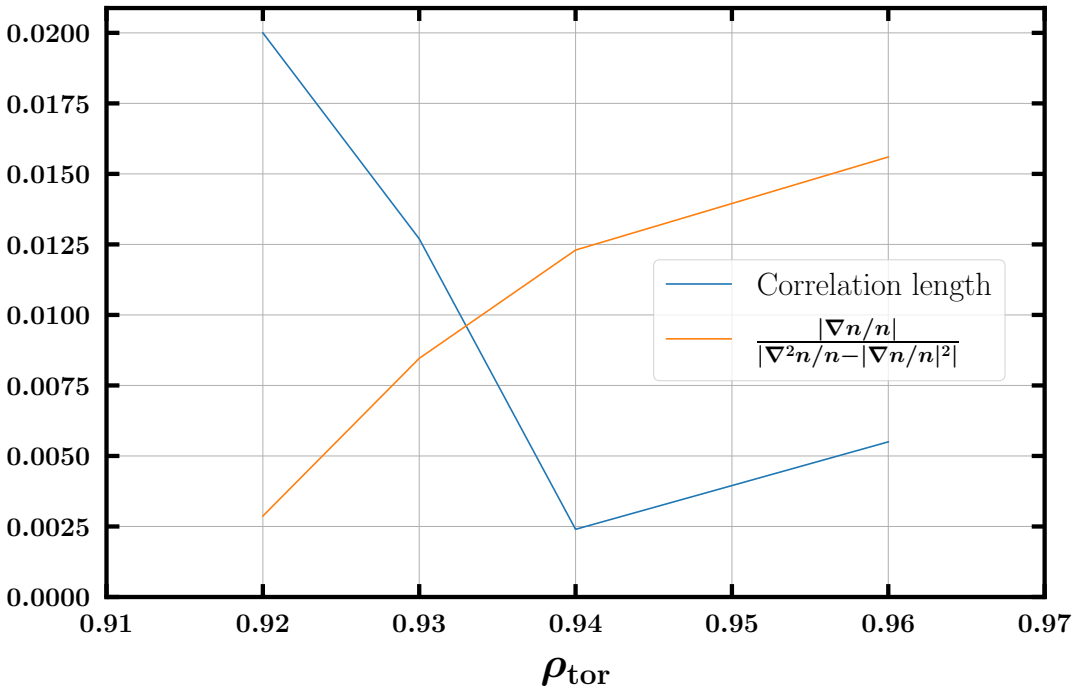

Figure 13: The condition $\Delta_x \ll |\frac{\nabla n_0}{n_0}|/|\frac{n_0\nabla^2 n_0 - (\nabla n_0)^2}{n_0^2}|$ is violated at $\rho_{\mathrm{tor}} = 0.92$ and 0.93 while being satisfied at $\rho_{\mathrm{tor}} = 0.94$ and 0.96. The local approximation is therefore invalid at $\rho_{\mathrm{tor}} = 0.92$ and 0.93.

remains an unresolved question, warranting future investigation. Based on the analysis conducted in this chapter, it is concluded that nonlocal effects are critical in the transition from the steep gradient region to the pedestal top.

3 Local Post-ELM Simulations

While the pre-ELM stage may be the most important due to its direct reflection of the pedestal structure (and its connection to confinement), we are also interested in the post-ELM stage, which reflects the recovery process of the pedestal. Again as Fig. 14 shows, three radial locations $\rho_{\mathrm{tor}} = 0.966, 0.976, 0.986$ that cover the upper pedestal to mid pedestal region are selected to study the ETG turbulence during post-ELM stage. Table 3 shows the physical input parameters for the simulations. All parameters except ω_{n} and ω_{T} are smaller than the pre-ELM analysis presented previously.

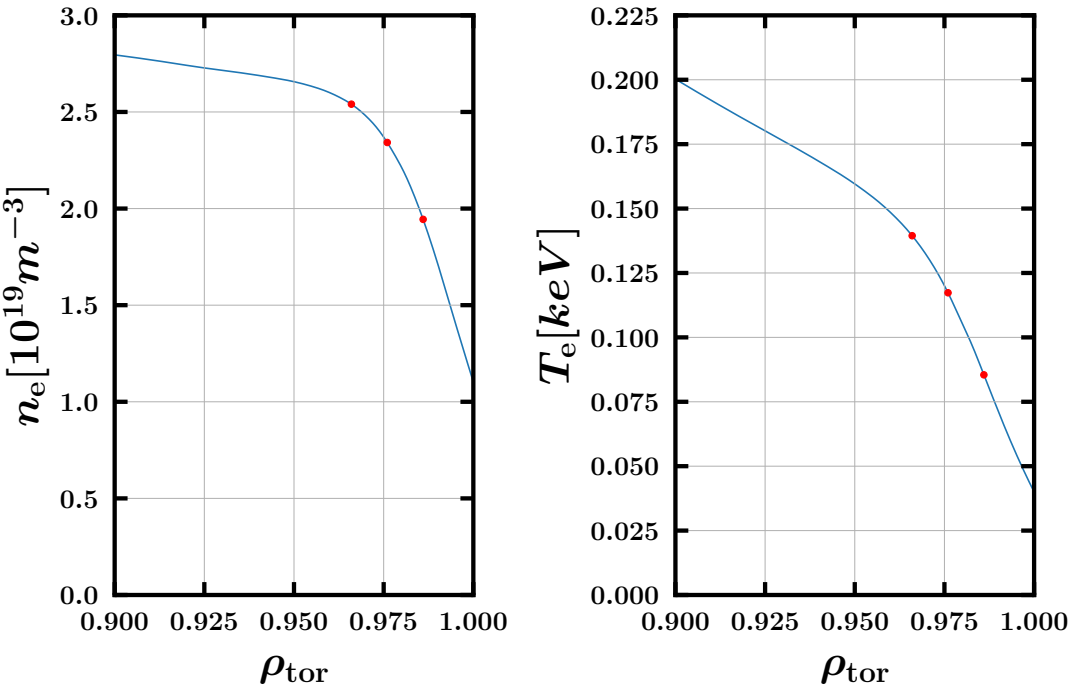

Figure 14: The electron density and temperature versus the normalized toroidal flux surface label $\rho_{\rm tor}$ during post-ELM stage.

ρ_{tor}	q_0	$\hat{s}$	$\omega_{\rm n}$	$\omega_{\rm T}$	η	β	$B_{\rm ref}$	$T_{\rm ref}$	$n_{\rm ref}$
0.966	6.72	4.71	4.98	12.5	2.51	0.0058	0.495	0.140	2.54
0.976	7.05	4.67	12.2	23.4	1.92	0.0045	0.495	0.117	2.34
0.986	7.41	4.98	27.0	41.2	1.53	0.0027	0.495	0.085	1.94

Table 3: The common physical input parameters at $\rho_{\rm tor} = 0.92, 0.94, 0.96$, respectively. η and β decrease as $\rho_{\rm tor}$ increases. Magnetic shear does not vary a lot around the pedestal top.

Figure 15 shows the growth rate spectrum at three different radial locations. The peak of the growth rate spectrum moves toward smaller scales as $\rho_{\rm tor}$ increases while the growth rate spectrum is similar at large scales. By utilizing simple mixing length estimates on the growth rate spectrum with similar k_x, we can naively expect ETG turbulence to be stronger at $\rho_{\rm tor} = 0.976$ than 0.986 since the growth rates for the former at large scales are a bit larger along with the fact that $T_{\rm ref}$ is also larger at this radial location. As for $\rho_{\rm tor} = 0.966$, it is not enough to predict whether ETG turbulence is more prominent here compare to 0.976 and 0.986 just by using simple mixing length estimates because the spectrum remains to be

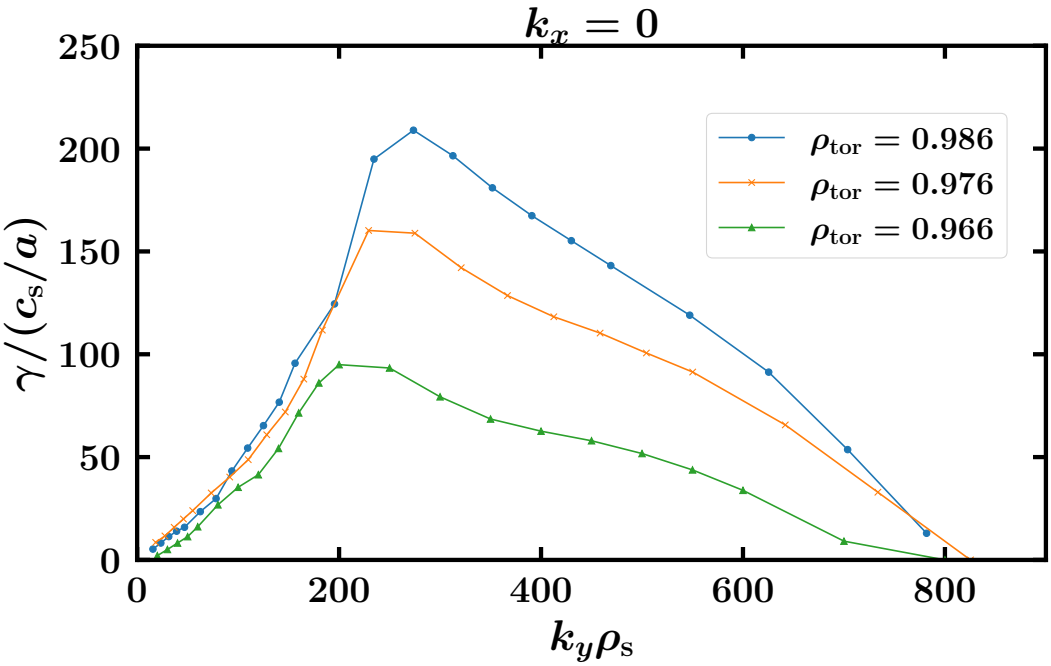

Figure 15: The growth rate spectrum for three radial locations $\rho_{\rm tor} = 0.966, 0.976, 0.986$ during the post-ELM stage with $c_{\rm s}$ and $\rho_{\rm s}$ calculated at $\rho_{\rm tor} = 0.966$. .

slightly below those from the two at large scales with larger $T_{\rm ref}$.

Figure 16 shows the heat fluxes calculated at these radial locations. It is not surprising, that the electron heat flux is small at $\rho_{\rm tor} = 0.986$ due to the low temperature and η. On the other hand, the ETG turbulence at $\rho_{\rm tor} = 0.976$ is produces 0.31MW of heat flux which is similar to the pre-ELM case at the pedestal top region $\rho_{\rm tor} = 0.94$, suggesting the ETG turbulence is pushed toward the core during the inter-ELM period. By comparing the profiles from Fig. 1 and Fig. 14, one can see that the temperature profiles are basically the same with the turning point or, the part with larger temperature profile curvature, straightened and moved from ~ 0.965 to ~ 0.94. On the contrary, the density profile keeps building up with the density on the pedestal top increases from $\sim 2.75 \times 10^{19} m^{-3}$ to $\sim 3.9 \times 10^{19} m^{-3}$during the period, while the turning point is pushed from ~ 0.97 to 0.94. This indicates that peak η around the pedestal top is pushed inward during the inter-ELM period. While it is known that the heat flux produced by ETG turbulence depends on η and $T_{\rm ref}$, it should also be

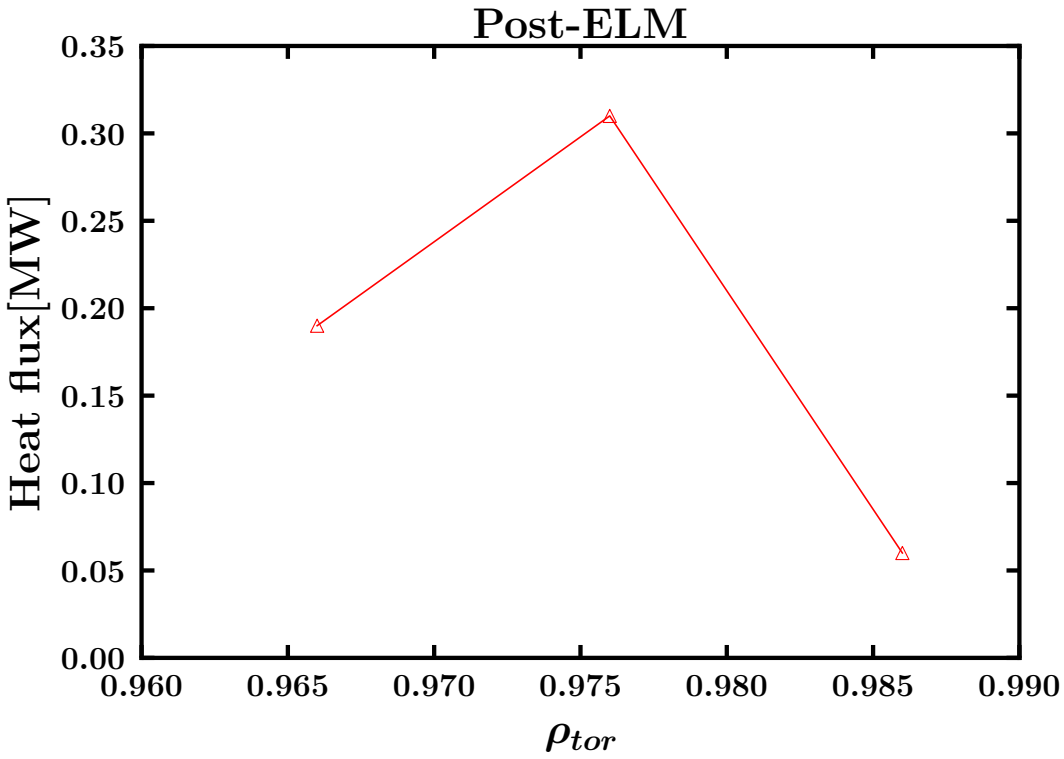

Figure 16: The growth rate spectrum for three radial locations $\rho_{\rm tor} = 0.966, 0.976, 0.986$ during the post-ELM stage.

pushed inward with its magnitude increased, which agrees with the result presented here.

The same thing is true for the post-ELM case as shown in Fig. 17. The only difference is that the instabilities are more sensitive to the gradients, with the growth rates at the larger scale doubled when there are 20% increase in $1/L_{\rm T0}$ and 20% decrease in $1/L_{\rm n0}$, implying that the heat flux produced by the ETG turbulence at this stage can reach a higher saturation level within the measurement error.

The heat fluxes obtained from nonlinear gyrokinetics simulations considering the post-ELM stage at radial locations of $\rho_{\rm tor} = 0.976$ is shown in Fig. 18. The simulations also show that the heat flux increases significantly when there is a 20% increase in $1/L_{\rm T0}$ and a 20% decrease in $1/L_{\rm n0}$. To be more precise, the post-ELM case shows a $\sim 300\%$ increase in heat flux, which is more dramatic than the case saw at $\rho_{\rm tor} = 0.94$ during the pre-ELM stage. Again, this value is much higher than expected from linear simulations, which shows

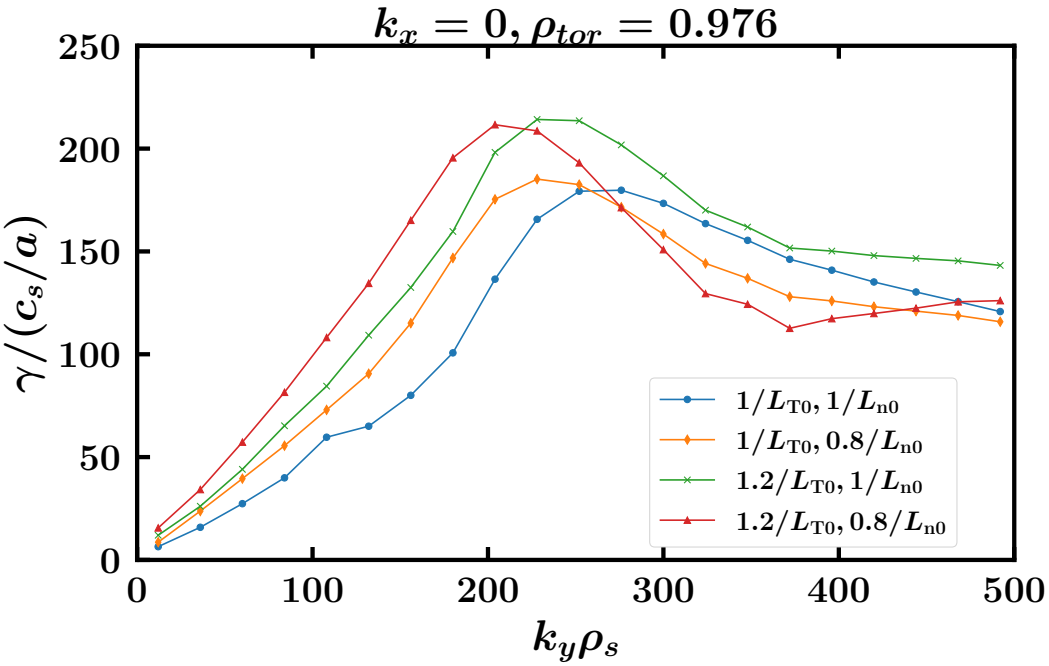

Figure 17: Growth rate spectrum at $\rho_{\rm tor} = 0.976$ during the post-ELM stage. The spectrum is moved upward about 60% when the temperature gradient $1/L_{\rm T0}$ is increased by 40%, and moved horizontally toward the larger scale when $1/L_{\rm n0}$ is decreased.

a growth rate increase of only $\sim 100\%$.

With regard to the fact that ETG is also shown to be active during pre-ELM stage around the upper pedestal to the pedestal top region, ETG can be regarded as excited during the inter-ELM period. Also, since both Fig. 5 and 18 show substantial heat flux increase when η is adjusted within the error bar, ETG turbulence is very likely to be playing an important role in pedestal formation in MAST.

4 Conclusion

This paper presents local and global gyrokinetic analysis of ETG turbulence and transport in the MAST pedestal. Our results suggest that ETG turbulence likely plays a significant role in transport in spherical tokamaks in the upper pedestal and pedestal top regions. This is true both in a pre-ELM phase prior to an ELM as well as a post-ELM phase when the pedestal

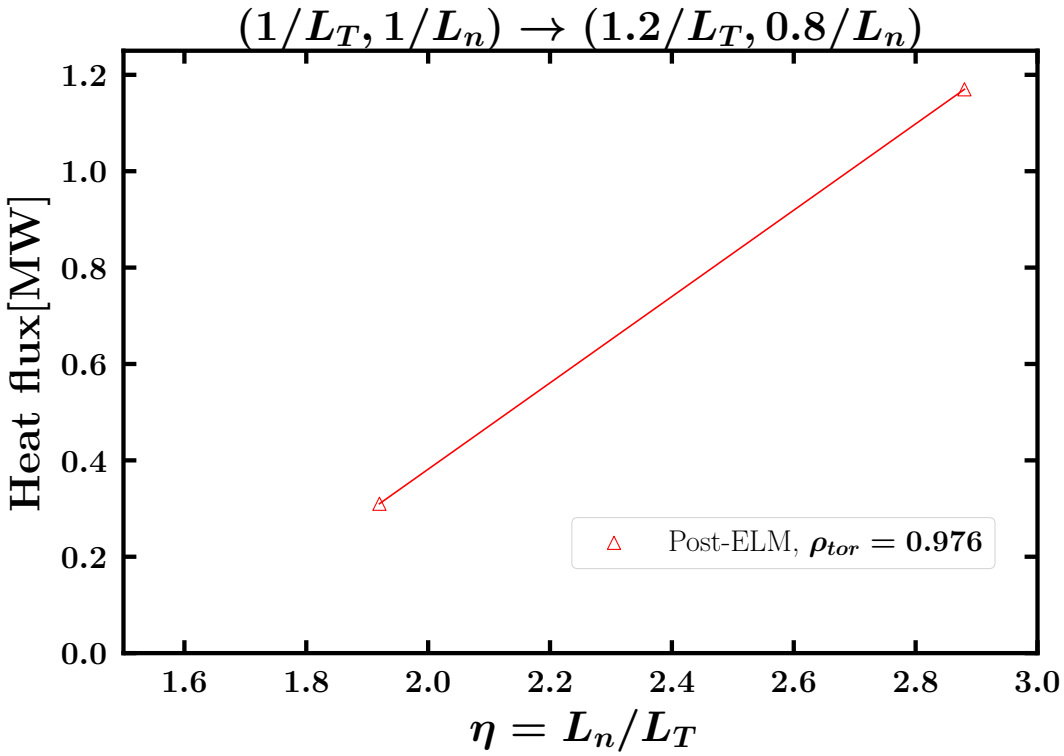

Figure 18: Heat fluxes calculated at $\rho_{\mathrm{tor}} = 0.976$ for the post-ELM stage shows the heat flux increased significantly when there is a 20% increase in $1/L_{\mathrm{T0}}$ and a 20% decrease in $1/L_{\mathrm{n0}}$. The amount of heat flux increased is more profound than the pre-ELM stage.

is recovering and the temperature profile is rebuilding. Simulations produce transport levels on the order of 1 MW (compared to 4 MW total heating power). The heat flux strongly increases with the temperature gradient, indicating stiff transport.

One major result of this paper is that the flux tube approximation breaks down at the pedestal top, where we observe that local simulations produce unrealistically high transport levels while global simulations recover reasonable transport levels similar to nearby points in the upper pedestal. We attribute the breakdown of the local approximation to large radial structures that emerge in the nonlinear simulations. Large-scale structures sample the entire structure of the equilibrium profile not just its local gradients. The pedestal top is precisely the location where the curvature of the profile may be a strong determinant of stability. The difference between the local and global stability of an eigenvalue problem is a well-known

phenomenon. An extreme case is when the system is locally unstable everywhere but is globally stable [28]. The breakdown of the flux tube approximation can be parameterized by the ratio of the radial correlation length to a length scale representative of profile curvature; the local and global simulations agree when this ratio is sufficiently smaller than unity. Whether the global effect is linear or nonlinear will be left for future research.

Overall, this study provides insight into the mechanisms behind the formation of the MAST pedestal and may inform strategies for optimizing the edge plasma of spherical tokamaks, thus enhancing confinement. Note that the study of the saturation mechanisms of the turbulence is left in Appendix A for further reading.

Acknowledgements

This work is supported by U.S. Department of Energy under grant No. DE-SC0019102, No. DE-FG02-04ER54742, and the EPSRC Energy Programme under grant No. EP/W006839/1.

Appendix A ETG Saturation Mechanism

In addition to determining the presence of ETG turbulence in the pedestal, it is important to investigate the mechanisms by which ETG turbulence reaches saturation within the pedestal. One can begin with the gyrokinetic equation for the perturbed distribution function $g_{j,k}$ (sometimes called the generalized distribution function) for species j (see Ref. [23] for details and normalizations). Its evolution is governed by the gyrokinetic Vlasov equation $\partial g_{j,k}/\partial t = L[g_{j,k}] + N[g_{j,k}]$, where L and N represent the linear and nonlinear operators, with

$$L[g_{j,k}] = -\omega_* F_{j0} i k_y \chi_{j,k} + \frac{\beta T_{j0}}{q_j B_0^2} v_\parallel^2 \omega_p \Gamma_{y,j,k} - \frac{v_{\mathrm{T}j}}{J B_0} v_\parallel \Gamma_{z,j,k}$$

$$- \frac{T_{j0}\left(2v_\parallel^2 + \mu B_0\right)}{q_j B_0}\left(K_y \Gamma_{y,j,k} + K_x \Gamma_{x,j,k}\right) + \frac{v_{\mathrm{T}j}}{2JB_0}\mu \partial_z B_0 \frac{\partial f_{j,k}}{\partial v_\parallel} + \langle C_{j,k}(f)\rangle\,, \tag{1}$$

and

$$N[g_{j,k}] = \sum_{k'}\left(k'_x k_y - k_x k'_y\right)\chi_{j,k'} g_{j,k''}\ , \tag{2}$$

where $\mathbf{k}'' = \mathbf{k} - \mathbf{k}' = (k_x - k'_x, k_y - k'_y)$, $\omega_* = \omega_{\mathrm{n},j,k} + \left(v_\parallel^2 + \mu B_0 - 3/2\right)\omega_{\mathrm{T},j,k}$, while $f_{j,k} = g_{j,k} - \frac{2q_j}{m_j v_{\mathrm{T}j}}\bar{A}_{\parallel,k}F_{j0}$ is the total perturbed distribution function, $\chi_{j,k} = \bar{\Phi}_k - v_{Tj}v_\parallel \bar{A}_{\parallel,k}$ is the modified potential, v_{Tj} is the species-dependent thermal velocity, $\bar{\Phi}_k$ is the gyroaveraged electric potential, $\bar{A}_{\parallel,k}$ is the gyroaveraged parallel magnetic potential, $v_\parallel$ is the parallel velocity, n_{j0} is the background density, T_{j0} is the background temperature, q_j is the charge, F_{j0} is the background Maxwellian, $\mathbf{v} = (v_\parallel, \mu)$ is the velocity vector, $\omega_p = a/L_p$ is the normalized pressure gradient, $K_{x,y}$ are the curvature terms, $\Gamma_{x,y} = ik_{x,y}g + \frac{q_j}{T_{j0}}F_{j0}ik_{x,y}\chi$, and $\Gamma_z = \partial_z g + \frac{q_j}{T_{j0}}F_{j0}\partial_z\chi + \frac{v_{\mathrm{T}j}q_j}{T_{j0}}v_\parallel \mu F_{j0}\bar{A}_{\parallel,k}\partial_z B_0$.

Note that $L[g_{j,k}]$ consists of the terms of gradient drive, pressure, parallel dynamics, curvature, trapping, and collisions in order. With the above definitions, one can define the energy exchange rate through nonlinearities $dE/dt|_{\mathrm{nl}}$, the energy injection rate from the drive $dE/dt|_{\mathrm{drive}}$, and collisional energy dissipation rate $dE/dt|_{\mathrm{col}}$, and the numerical energy dissipation rate $dE/dt|_{\mathrm{diss}}$ in the total time derivative of the energy $dE_{\mathrm{tot},k}/dt$ at wavenumber k as

$$\begin{aligned}
\frac{dE_k}{dt}\Big|_{\mathrm{nl}} &= 2\mathrm{Re}\left\{\sum_{k',j}\int \frac{n_{j0}T_{j0}}{F_{j0}}\left[g_{j,k} + \frac{q_j F_{j0}}{T_{j0}}\chi_{j,k}\right]^*\left(k'_x k_y - k_x k'_y\right)\chi_{j,k'}g_{j,k''}dzdv\right\} \\
\frac{dE_k}{dt}\Big|_{\mathrm{drive}} &= -2\mathrm{Re}\left\{\sum_j \int \pi n_{j0}T_{j0}ik_y\nu_* g^*_{j,k}\chi_{j,k}dzdv\right\} \\
\frac{dE_k}{dt}\Big|_{\{\mathrm{diss,col}\}} &= -2\mathrm{Re}\left\{\sum_j \int \pi n_{j0}T_{j0}\Gamma^*_{j,k}C_{\{\mathrm{diss,col}\}j,k}(f)dzdv\right\},
\end{aligned} \tag{3}$$

where $\Gamma_{j,k} = f_{j,k} + \frac{q_j F_{j0}}{T_{j0}}\bar{\phi}$, and the non-conservative rate of change of energy $dE/dt|_{\mathrm{nc}}$ is the sum of $dE/dt|_{\mathrm{diss}}$, $dE/dt|_{\mathrm{drive}}$, and $dE/dt|_{\mathrm{col}}$ [24, 25]. In this section of the appendix, we focus on the saturated state at $\rho_{\mathrm{tor}} = 0.94$ for the pre-ELM stage and $\rho_{\mathrm{tor}} = 0.976$ for the post-ELM stage by doing similar triplet diagnostics and energy transfer analysis presented in [25].

The contour plots depicted in Fig. 19 offer valuable insights into the time-averaged energy flow in k-space during the saturation of ETG turbulence at $\rho_{\mathrm{tor}} = 0.94$ in the pre-ELM

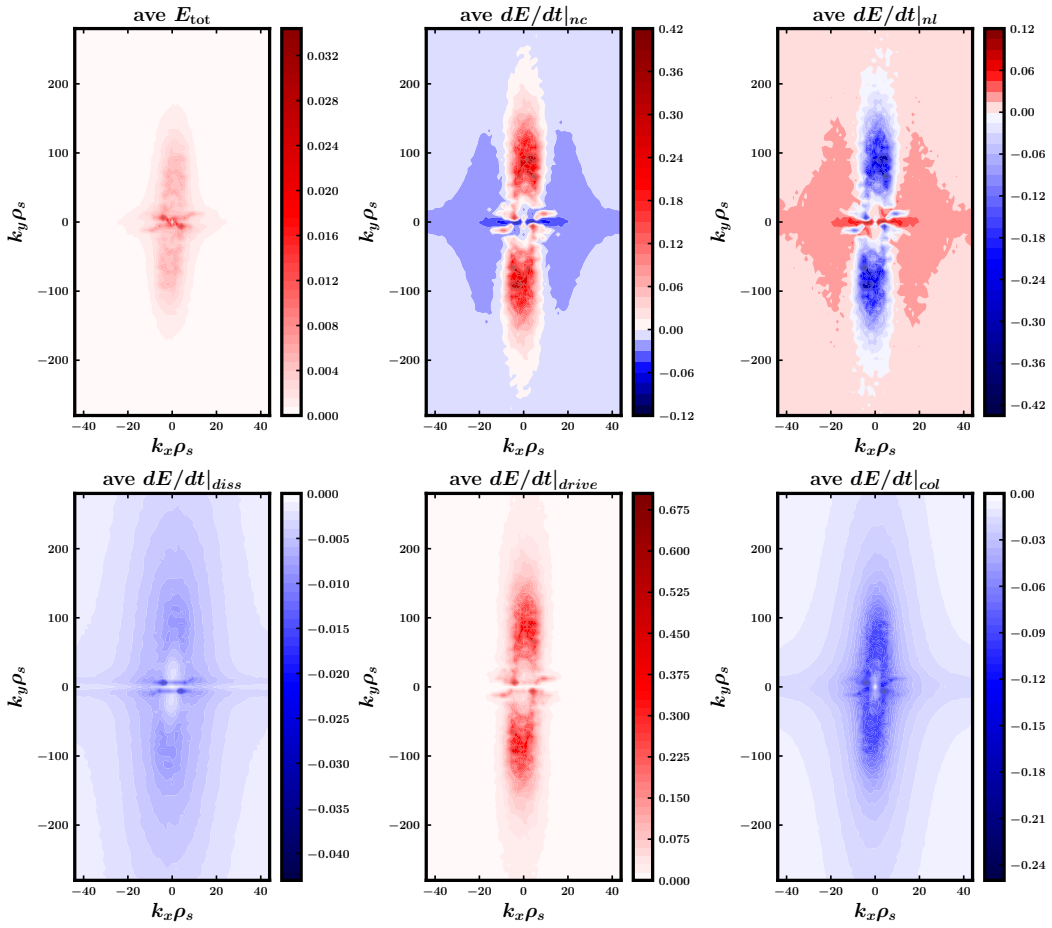

Figure 19: The energy and dE/dt contour plots at $\rho_{\rm tor} = 0.94$ during the pre-ELM stage. The $E|_{\rm tot}$ contour plot shows the streamers are excited, with $dE/dt|_{\rm drive}$ contour plot showing them injecting energy into the system. The energy is distributed across all scales via nonlinear processes and removed by collisions at all scales according to the $dE/dt|_{\rm nl}$ and $dE/dt|_{\rm col}$ contour plots. $dE/dt|_{\rm nc}$ contour plot shows forward and backward energy cascades are present.

stage. The contour plot for $E|$tot reveals strong excitation of low kx modes with $k_y \lesssim 180$, which aligns with the expected behavior since energy injection predominantly occurs within this range, as indicated by the $dE/dt|$drive contour plot. Subsequently, nonlinear processes redistribute the energy across all scales, as observed in the $dE/dt|$nl contour plot.

One can also observe that a tilted $E|_{\rm tot}$ contour plot in our simulation results. Analysis revealed that this phenomenon is a result of the E $\times$ B shear. However, it is expected that the magnitude of this effect was not sufficient to suppress the ETG turbulence, as the

growth rates of the low k_x modes are significantly larger ($\gtrsim 1$) than the E $\times$ B shearing rate $\gamma_{\mathrm{E}\times\mathrm{B}} = -0.311$.

The primary mechanism for the dissipation of the energy is through collisions which dominate over numerical dissipation. Analysis of the $dE/dt|_{\mathrm{nc}}$ contour plot reveals substantial energy removal at both small and large-scale ranges. From Fig. 2, one can find that the growth rate in the large-scale range is non-zero, suggesting that large-scale stable modes are also excited which leads to net energy removal in this range. Additionally, zonal modes are observed removing energy actively, though not the dominant energy sink for the saturation balance, through damping.

While it is commonly assumed that the primary mechanism for energy dissipation is through the forward cascade, the data presented in Fig. 19 suggests that inverse cascade and zonal mode damping also contribute to some level of energy removal. Note that the inverse energy cascade for ETG turbulence is also observed in various cases [22, 25].

While zonal modes are actively dissipating energy, does zonal-flow catalyzed nonlinear energy transfer plays an important role in saturating ETG turbulence? From the total energy contour plot in figure 19, one can see that zonal modes are excited but not prominent relative to the low k_x modes, therefore, zonal flow-catalyzed energy transfer might not be conspicuous. Figure 20 shows the nonlinear transfer rate $T_{\mathrm{nl},k}$ contour plots for six different wavenumbers where $T_{\mathrm{nl},k}$ is defined as

$$T_{\mathrm{nl},k} = 2\mathrm{Re}\left\{\sum_j \int \frac{n_{j0}T_{j0}}{F_{j0}}\left[g_{j,k} + \frac{q_j F_{j0}}{T_{j0}}\chi_{j,k}\right]^* \left(k'_x k_y - k_x k'_y\right)\chi_{j,k'} g_{j,k''} dz dv\right\}. \tag{4}$$

For the large-scale streamer at $k = (0, 6)$, it mostly interacts with modes with similar k_y at low k_x; energy is transferred to it from the highly excited unstable modes around $k = (4.3, -12)$ and $k = (-4.3, 12)$. However, no sign shows the modes at $k = (0, 6)$ strongly interact with zonal modes. The backward cascade observed from the $dE/dt|_{\mathrm{nc}}$ contour plot in Fig. 19 is therefore majorly driven by the large scale unstable modes with non-zero k_x.

For small-scale streamers at $k = (0, 30)$ and $(0, 102)$, the magnitude of the outgoing energy transfer represented by blue regions in the contour plot of $T_{\mathrm{nl},k}$ is broadly distributed

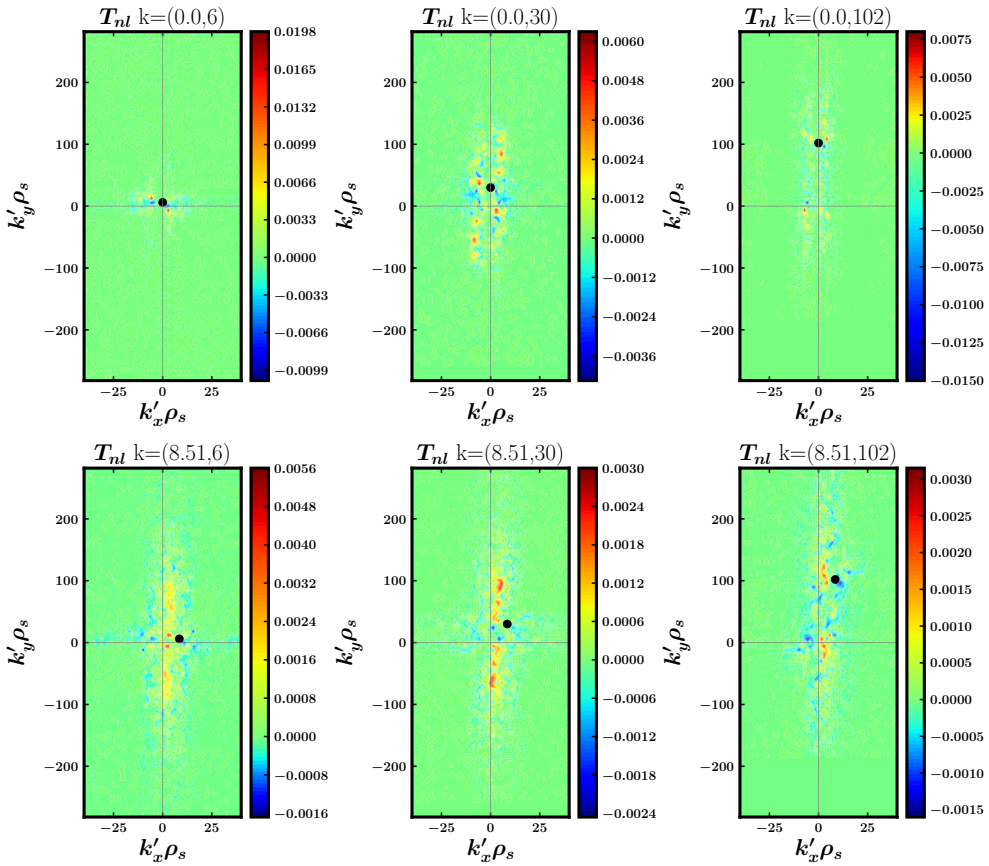

Figure 20: Triplet diagnostics $T_{\mathrm{nl},k}$ for various wavenumbers at $\rho_{\mathrm{tor}} = 0.94$ during pre-ELM satge. The $k = (0, 0.6)$ contour plot shows backward energy cascade is driven by large-scale $k_x \neq 0$ modes. Other contour plots show typical forward energy cascade is present.

at lower $k'_y < k_y$ denoting an inverse cascade. In terms of the radial scales it peaks at $k'_x \sim \pm 4.2$ with k'_y.

The $T_{\mathrm{nl},k}$ contour plots for $k = (8.51, 6)$, $(8.51, 30)$, and $(8.51, 102)$ show the sidebands are strongly interacting with lower k_x modes (i.e. the red regions are at lower k'_x) by carrying away energy (i.e. the blue regions are at higher k'_x. This is a clear sign ofa forward energy cascade in the radial direction. Again, the sidebands do not strongly interact with the zonal modes, both the forward and backward energy cascade observed in $dE/dt|_{\mathrm{nc}}$ contour plot in Fig. 19 are mostly driven by non-zonal catalyzed interactions. The ETG turbulence at $\rho_{\mathrm{tor}} = 0.94$ is therefore still mostly saturated by forward cascade in the radial direction with to small-scale stable regions as energy sinks, while there is inverse transfer to large-scale

	ρ_{tor}	n_x	n_{k_y}	n_z	n_w	$k_{y,min}\rho_s$	L_x
Local Pre-ELM							
	0.92	64	32	64	16	6	27.0
	0.93	64	96	96	16	2	10.9
	0.94	64	192	84	16	2	4.11
	0.96	64	256	84	16	2	4.05
Global Pre-ELM							
	0.905-0.975	256	48	64	16	12.04	15
Local Post-ELM							
	0.966	128	48	256	16	12	3.98
	0.976	128	64	280	24	12	4.39
	0.986	128	48	512	32	12	4.4

Table 4: Resolutions used for different nonlinear runs. $k_{y,min}$ is set to 6 for pre-ELM simulation at ρ_{tor} to avoid MTMs that keep the turbulence away from saturation. n_w is set to 32, which is exceptionally high for post-ELM simulation at $\rho_{\text{tor}} = 0.986$ to avoid positive energy injection from collision raised from numerical issue.

stable modes and zonal modes in the binormal direction.

Appendix B Simulation Setup

Table 4 presents the resolutions utilized in various nonlinear simulations. The table includes the following parameters: ρ_{tor}, which represents the radial location; n, denoting the number of grids; and L, indicating the box size. The subscripts used for n and L are as follows: s for specie, x for the radial direction, y for the bi-normal direction, z for the parallel direction, v for the parallel velocity space, and w for the magnetic moment. Moreover, $k_{y,min}\rho_s$ represents the minimum wavenumber in the bi-normal direction.

For all simulations, certain values remain the same and are not explicitly displayed in the table. These include $n_s = 2$, $n_v = 36$, $L_v = 3$, and $L_w = 9$. The Arakawa_zv is on to incorporate parallel and parallel velocity derivatives within a Poisson bracket structure and is solved using an Arakawa scheme.

Note that simulations conducted at outer radial locations necessitate higher n_z values, especially during the post-ELM period. Additionally, for enhanced resolution at the outboard mid-plane, the parameter edge_opt is set to 8. It is important to mention that the calculated

saturated heat fluxes for the pre-ELM cases, using $k_{y,min} = 6$ and 12, exhibit an error within 10%. Simulations with $k_{y,min} = 2$ are carried out to investigate the impact of close-ion-scale ETG modes. In most simulations, the saturated heat flux remains relatively unaffected, except for the case at $\rho_{\text{tor}} = 0.92$, where MTMs become dominant and do not exhibit turbulence saturation. It is also important to note that the simulations were ran on various machines, each with either 56 or 64 cores per node. Consequently, the choice of n_z values is based on selecting multiples of 7 or 8 to effectively utilize the computational power of these supercomputers.

In the post-ELM (Edge Localized Mode) simulation at $\rho_{\text{tor}} = 0.986$, a high n_w resolution is employed to mitigate positive energy input resulting from collisions caused by numerical errors.

References

[1] W. Guttenfelder et al., Nucl. Fusion **62**, 042023 (2022)

[2] F. Wagner et al., Phys. Rev. Lett. **49**, 1408 (1982).

[3] J.W. Connor, Plasma Phys. Controlled Fusion **40**, 531 (1998).

[4] F. Jenko, Comp. Phys. Commun. **125**, 196 (2000).

[5] W. Dorland, F. Jenko, M. Kotschenreuther, and B. N. Rogers, Phys. Rev. Lett. **85**, 5579 (2000).

[6] F. Jenko and W. Dorland, Phys. Rev. Lett. **89**, 225001 (2002).

[7] F. Jenko, Phys. of Plasmas **16**, 055901 (2009).

[8] D. R. Hatch, D. Told, F. Jenko, H. Doerk, M. G. Dunne, E. Wolfrum, E. Viezzer, and M. J. Pueschel, Nucl. Fusion **55**, 063028 (2015).

[9] D. Hatch, M. Kotschenreuther, S. Mahajan, P. Valanju, and X. Liu, Nucl. Fusion **57**, 036020 (2017).

[10] D. Hatch, M. Kotschenreuther, S. Mahajan, G. Merlo, A. Field, C. Giroud, J. Hillesheim, C. Maggi, C. P. von Thun, C. Roach, and S. S., Nucl. Fusion **59**, 086056 (2019).

[11] D. R. Hatch, C. Michoski, D. Kuang, B. Chapman-Oplopoiou, M. Curie, M. Halfmoon, E. Hassan, M. Kotschenreuther, S. M. Mahajan, G. Merlo, M. J. Pueschel, J. Walker, and C. D. Stephens, Phys. of Plasmas **29**, 062501 (2022).

[12] W. Guttenfelder, R. Groebner, J. Canik, B. Grierson, E. Belli, and J. Candy, Nucl. Fusion **61**, 056005 (2021).

[13] B. Chapman-Oplopoiou, D. R. Hatch, A. R. Field, L. Frassinetti, J. Hillesheim, L. Horvath, C. F. Maggi, J. Parisi, C. M. Roach, S. Saarelma, and J. Walker, Nucl. Fusion **62**, 086028 (2022).

[14] D. Told, Gyrokinetic microturbulence in transport barriers, Ph.D. thesis, Universität Ulm (2012).

[15] D. Dickinson, C. M. Roach, S. Saarelma, R. Scannell, A. Kirk, and H. R. Wilson, Phys. Rev. Lett. **108**, 135002 (2012).

[16] D. Dickinson, C. M. Roach, S. Saarelma, R. Scannell, A. Kirk, and H. R. Wilson, Plasma Phys. Control. Fusion **55**, 074006 (2013).

[17] D. R. Hatch, M. Kotschenreuther, S. Mahajan, P. Valanju, F. Jenko, D. Told, T. Görler and S. Saarelma, Nucl. Fusion **56** , 104003 (2016).

[18] M. J. Pueschel, D. R. Hatch, M. Kotschenreuther, A. Ishizawa, and G. Merlo, Nucl. Fusion **60**, 124005 (2020).

[19] Ehab Hassan, D. R. Hatch, M. R. Halfmoon, M. Curie, M. T. Kotchenreuther, S. M. Mahajan, G. Merlo, R. J. Groebner, A. O. Nelson, and A. Diallo, Nucl. Fusion **62**, 026008 (2022).

[20] M. Kotschenreuther et al, Nucl. Fusion **59**, 096001 (2019).

[21] M. Landreman and D. R. Ernst, Plasma Phys. Control. Fusion **54**, 115006 (2012).

[22] Z. Lin, L. Chen, F. Zonca, Phys. of Plasmas **12**, 056125 (2005).

[23] M. J. Pueschel, F. Jenko, D. Told, and J. Büchner, Phys. Plasmas **18**, 112102 (2011).

[24] D. R. Hatch, Ph.D. Thesis, *Mode Analyses of Gyrokinetic Simulations of Plasma Microturbulence*, University of Wisconsin-Madison (2010).

[25] J. Walker, D. R. Hatch, (2023). *ETG turbulence in a tokamak pedestal*, Institution for Fusion Studies, The University of Texas at Austin.

[26] J. Candy, E. A. Belli, and G. Staebler, Plasma Phys. Control. Fusion **62**, 042001 (2020).

[27] F. Parra1 and M. Barnes, Plasma Phys. Control. Fusion **57**, 054003 (2015).

[28] S. M. Mahajan and V. Krishan, ApJ **682**, 602 (2008).